Mechanisms Governing Early-Age Structural Evolution in Alkali-Activated Low-Grade Calcined Clays

Neel Bhuskute[a] and Sriramya Duddukuri Nair[b*]

[a]School of Civil and Environmental Engineering, Cornell University, 527 College Ave, Ithaca, NY 14853, USA. nb642@cornell.edu

[b]School of Civil and Environmental Engineering, Cornell University, 527 College Ave, Ithaca, NY 14853, USA. sn599@cornell.edu

[*]Corresponding author: Sriramya Duddukuri Nair

Abstract

Expanding alkali-activated clays beyond high-purity metakaolin requires the use of low-grade calcined clays (LCCs), whose variable mineralogy and reactivity will influence fresh-state evolution, setting behavior, and strength development. This work investigates the mechanisms governing early-age structural evolution of three alkali-activated LCCs and one high-purity metakaolin (MK) by linking chemical transformations to rheological development. All systems exhibited a consistent four-stage viscoelastic evolution in small amplitude oscillatory shear (SAOS) tests, indicating a common structural pathway despite differences in precursor composition. The transition at the end of stage III corresponded to the formation of a solid product and aligned closely with measured set times, providing a reliable rheological indicator of setting. Deconvolution of the time-resolved FTIR scans identified the lower-wavenumber, LW band, (900-950 cm^{-1}) as the most sensitive marker of precursor-specific chemical evolution. Coupling this LW band with SAOS results produced characteristic chemical-to-rheological evolution curves that distinguished the precursors by reaction rate and degree of Si-O-Si/Al peak shift. These trajectories showed the differences in spectral evolution preceding rapid stiffening, and how impurity content and reactive fraction may influence each system as it transitions into a connected network. Total heat from isothermal calorimetry provided a strong comparative indicator for performance of the precursors. This integrated mechanistic framework provides a practical route for interpreting variable LCC feedstocks and designing alkali-activated clay binders with controlled workability, setting, and strength.

Keywords: rheology; viscoelastic evolution; low-grade calcined clays (LCCs); alkali-activated materials (AAMs); structure-property relationships;

1. Introduction

Alkali-activated materials (AAMs) have been widely discussed as a promising alternative to ordinary portland cement (OPC) forming hardened binders through dissolution and polycondensation of aluminosilicate precursors in alkaline environments. Although fundamentally different from the hydration reactions in OPC binders, it still produces a compact microstructure, making AAMs suitable for similar applications. Common precursors include fly ash, ground granulated blast furnace slag, and calcined clays, with kaolinite-based materials being particularly attractive due to their relatively low calcination temperature (~750 °C) and reduced associated emissions [1], [2].

Among these, metakaolin (MK) has been extensively studied as a model precursor due to its high amorphous content and reactivity, enabling the development of AAM systems with excellent mechanical and durability performance [1], [3]-[9]. However, the use of high-purity MK is limited by feedstock availability, cost, and its fine particle size which leads to high water demand and poor workability [10] - [12]. These limitations motivate the use of low-grade calcined clays (LCCs), which are more abundant, less processed, and potentially more sustainable.

Despite these advantages, LCCs exhibit significant variability in chemical composition, mineralogy, amorphous content, and particle size, all of which influence dissolution behavior, reaction kinetics, and network formation. While previous studies have examined the effects of mixture design parameters such as Si/Al ratio, Na/Al ratio, and curing conditions [13] - [16], they have largely focused on high-purity systems and do not fully capture the variability inherent to low-grade clays. As a result, the structure-property relationships governing early-age behavior in LCC-based alkali-activated systems remain insufficiently understood.

The alkali activation mechanism involves dissolution of aluminosilicate species (Fig. 1), followed by oligomer formation and polycondensation into a hardened network [17], [18]. Variations in precursor composition, particularly Si/Al ratio and amorphous content, influence the extent of reaction [13], [19] - [22], while crystalline impurities such as quartz and mullite may reduce the reactive fraction [23] - [26]. Activator chemistry, including Na/Al ratio and silica modulus, further governs dissolution kinetics and network development. However, most existing studies focus on end-point properties such as strength, providing limited insight into the evolution of structure during the early stages of reaction. In particular, the link between chemical evolution and rheological behavior, which governs workability and setting, remains underexplored for LCC systems.

Fresh-state behavior is critical for processing and applications such as extrusion-based construction and additive manufacturing. Conventional tests provide limited insight into structural evolution, necessitating advanced rheological approaches. Small-amplitude oscillatory shear (SAOS) enables tracking of viscoelastic evolution and identification of structural transitions during setting. However, its application to LCC systems, particularly in combination with chemical techniques such as *in situ* FTIR, remains limited. In this study, the early-age behavior of alkali-

activated pastes derived from three low-grade calcined clays and a reference metakaolin is investigated using an integrated approach combining rheology, isothermal calorimetry, FTIR, and mechanical testing. The objective is to link chemical evolution to rheological development and identify common features in structural evolution across systems of varying reactivity. This work aims to provide a clearer mechanistic understanding of LCC-based alkali activation and support improved mixture design using variable clay resources.

2. Materials and Methods

2.1 Materials

Four clays with different geographical sources and calcination methods were used as precursors in this study. The precursor for the control sample was pure MK, obtained from BASF. Three commercial LCC precursors were procured from different geographical sources. The chemical composition of all four precursor clays is summarized in Table 1. The D_{10}, D_{50}, and D_{90} values of all clays are listed in Table 2. pMK was observed to be considerably finer compared to the pLCCs. Fig. 1 shows the particle shapes for the four clays obtained using a Scanning Electron Microscope. The clays are observed to only vary in size while having similar shapes and surface texture.

Table 1: Chemical compositions (oxide analysis) of the precursor (p) clays.

	pLCC-1	pLCC-2	pLCC-3	pMK
SiO_2	54.59	44.33	68.90	48.7
Al_2O_3	35.31	41.96	16.58	42.88
Fe_2O_3	3.09	1.1	4.87	2.09
CaO	0.5	1.12	0.45	0.34
MgO	0.27	0.15	0.65	0.41
SO_3	0.04	0.4	0.23	0.21
Na_2O	0.03	0.05	0.26	0.17
K_2O	0.98	0.12	1.21	0.16
TiO_2	1.79	1.91	0.93	1.64
P_2O_5	0.11	0.02	0.08	0.05
Mn_2O_3	0.03	0	0.02	0
SrO	0.04	0	0.01	0
LOI	3.15	0.84	5.41	0.6

Table 2: Particle size distribution of the precursor clays.

	pLCC-1	pLCC-2	pLCC-3	pMK
D_{10} (µm)	2.12	1.74	2.12	1.83
D_{50} (µm)	10.42	10.53	10.26	6.23
D_{90} (µm)	30.23	38.98	30.83	16.04

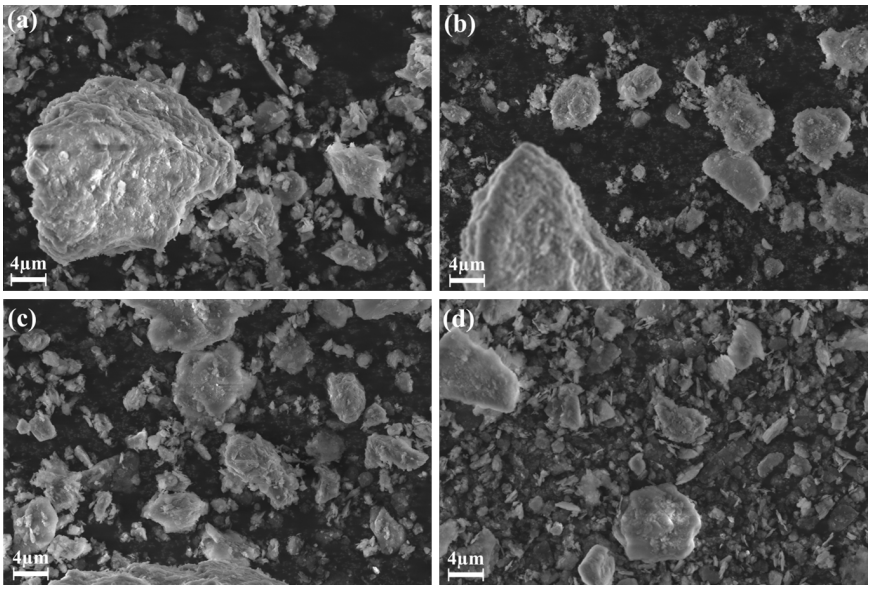

Figure 1: Particle shape and morphology of (a) pLCC-1, (b) pLCC-2, (c) pLCC-3, and (d) pMK precursors.

The mineralogical composition of the clays, determined through XRD analysis, is presented in Fig. 1. All XRD measurements were performed using a Bruker D8 diffractometer equipped with Cu Kα radiation (λ = 1.54 Å). The instrument was operated at 40 kV and 25 mA, and scans were collected over a 2θ range of 5° to 70°. A 10 percent Rutile internal standard was added to each sample to quantify the approximate amorphous fraction, which was calculated using the PROFEX software and is reported in Fig. 2. The measured amorphous content was taken as an estimate of the reactive phase of each clay, consistent with previous studies that use amorphous fraction as a key indicator of reactivity [27], [28].

Alkaline activator was prepared by blending sodium hydroxide (NaOH) and commercially available sodium silicate solution (Na_2SiO_3). NaOH stock solution was first prepared and allowed to cool to room temperature. The sodium silicate solution (PQ Corp solution D), containing 15% Na_2O, 30.5% SiO_2, and 55% H_2O, was then added to the prepared NaOH solution according to proportions in Table 3 under constant stirring and then continuously stirred for 24 hours to ensure homogeneity. Activator compositions were adjusted to achieve target silica modulus (SM = SiO_2/Na_2O molar ratio) with mixing proportions for each blend summarized in Table 3. The water-to-binder (w/b, where binder refers to the precursor) ratio was chosen using rheological flow measurements to ensure workable pastes. It was kept constant at 0.6 for all LCC-based mixtures. Pure MK was not workable at this w/b ratio, and after several trials, the lowest workable ratio was identified as 0.9 and was used for all MK-based mixtures.

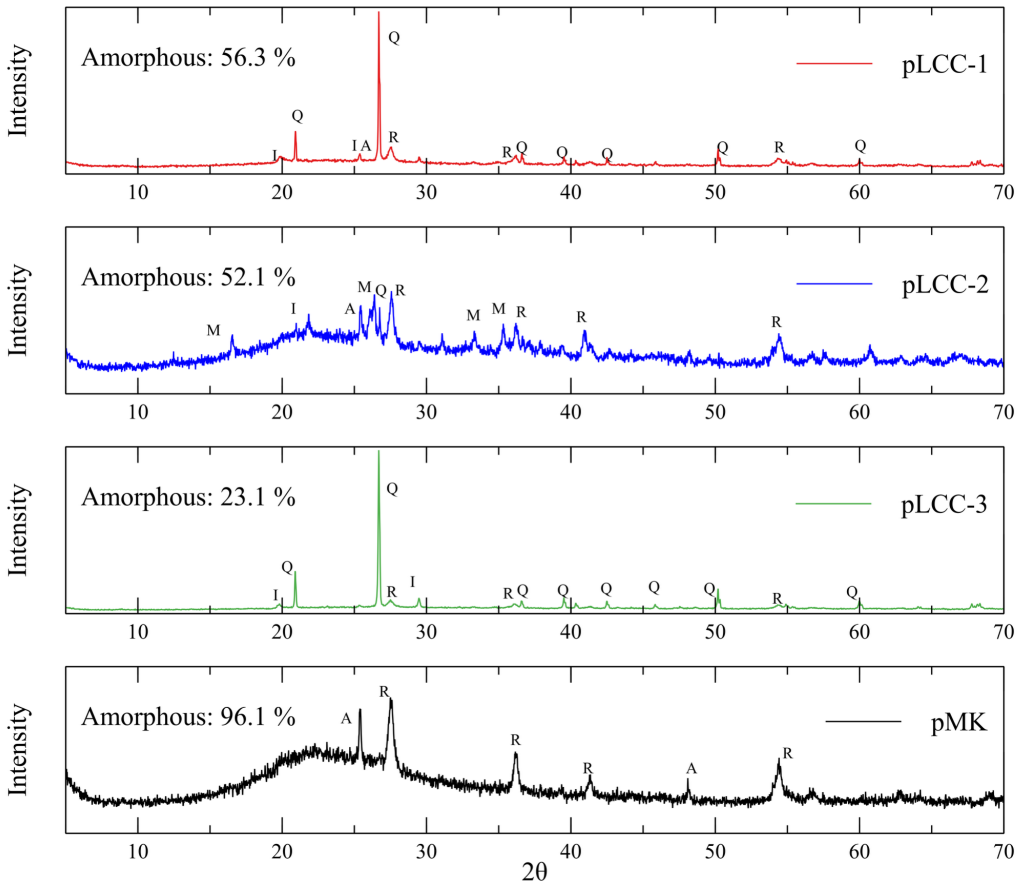

Figure 2: Mineralogical composition of the precursor clays (10% internal standard – Rutile). Q – Quartz, A – Anatase, C – Calcite, M – Mullite, I – Illite-smectite, R – Rutile.

Table 3: Mixing proportions for the alkali activated pastes.

	LCC-1	LCC-2	LCC-3	MK	LCC-1 SM0.75	LCC-1 SM1.25
Precursor (g)	500	500	500	400	500	500
NaOH (g)	64.7	64.7	64.7	77.7	86.8	46.2
Water (g)	138.3	138.3	138.3	166	165.3	115.5
Sodium Silicate Sol. (g)	296.9	296.9	296.9	356.2	274.9	338.2
Activator (Total) (g)	499.9	499.9	499.9	599.9	499.9	499.9
Water-binder (w/b)	0.6	0.6	0.6	0.9	0.6	0.6
Silica Modulus (SM)	1.00	1.00	1.00	1.0	0.75	1.25
Si/Al (paste)	1.74	1.23	4.44	1.5	1.67	1.81
Na/Al (paste)	0.88	0.74	1.89	1.09	0.97	0.8
Note: Weights per 1 kg paste						

Pastes were prepared in small batches (~30 g) using a high-shear handheld mixer (modified frother, up to 12,000 rpm). Precursor and activator were first hand-mixed for 30 s, followed by 90 s of high-shear mixing and 15 s vortex mixing to ensure homogenization. Mixing was completed

within ~2–3 min, after which the paste was immediately used for testing. Activator solutions were prepared within one week of use and stored in sealed containers to prevent precipitation.

2.2 Experimental Methods

2.2.1 Rheological Testing

Rheological measurements were performed using an Anton Paar MCR 302 rheometer with a 20 mm serrated parallel plate geometry under controlled temperature and humidity conditions. Four rheological measurements were carried out on the alkali-activated clay pastes: flow curves, time sweeps, amplitude sweeps and frequency sweeps. Prior to these tests, each sample was first presheared at 100 s^{-1} for 30 s followed by a rest period at 30 s.

Flow curves were obtained to determine the yield stress and plastic viscosity of freshly mixed pastes. The flow test profile consisted of a stepwise ramp-up of shear rate from 10-100 s^{-1} in 6 steps and a ramp-down to 10 s^{-1} in 5 steps. To reach a stable shear stress value with time, 5 shear stress points were recorded at every shear rate value. The last recorded point at every step within the ramp-down regime was fitted using the Bingham model (Equation 1) for LCC mixtures:

$$\tau = \tau_o + \eta\dot{\gamma} \quad \text{(Equation 1)}$$

where η is the plastic viscosity (Pa.s), τ is the shear stress (Pa), τ_o is the yield stress (Pa) and $\dot{\gamma}$ is the shear rate (s^{-1}). The yield stress and the viscosity also help to get a quantitative measurement indicating workability of the mixture.

Viscoelastic evolution was monitored using the SAOS tests within the linear viscoelastic domain (LVED). If stress exceeds the LVED, the strain response becomes nonlinear and no longer reflects the true reaction mechanism. To ensure that the testing stayed within the LVED, a frequency sweep (0.1–10 Hz at 0.01% strain) and an amplitude sweep (0.005% - 10% strain at 1 Hz) was performed. A frequency of 1 Hz and an amplitude of 0.01%, seen to be consistent with literature values (1–1.6 Hz & 0.005 – 0.1%) for testing the AAMs, was selected for SAOS tests [29]. Wet sponges were placed under the hood next to the samples to maintain humidity and prevent drying. The set time of the AAM pastes was measured using the Vicat needle apparatus specified in ASTM C191 without considering normal consistency to maintain the same w/b ratios for all the LCCs [30]

2.2.2 Isothermal Calorimetry

Isothermal calorimetry (IC) was used to monitor the heat flow of the AAM pastes, providing insight into both the heat evolution and the extent of the geopolymerization reaction over time. After preparing the pastes as described in Section 2.1, samples were placed in a TAM Air isothermal calorimeter (TA Instruments) at 25 °C. Deionized water was used as the reference material for all samples. Data was collected continuously for seven days, and the recorded heat flow profiles were used to track the progression of the reaction. IC was also used to measure the reactivity of the 4 precursors using the modified rapid, relevant and reliable (MR^3) test based on Suraneni et. al. [31].

2.2.3 Compressive Strength

Compressive strength testing was carried out to assess the performance. Cylinders of 6 mm diameter × 12 mm length were cast for each mixture using silicone rubber molds (Mold Max 40). The cylinders were cured in an environmental chamber at the required temperature and 100% RH. On day 7 the cylinders were subjected to uniaxial compressive loading using an MTS EXCEED electromechanical load frame with a 5 kN load cell and at an applied strain rate of 0.002. A minimum of 6 cylinders were tested for each paste mixture.

2.2.4 Fourier Transform Infrared Spectroscopy

The chemical evolution of the pastes was examined using an Attenuated Total Reflectance Fourier Transform Infrared (ATR-FTIR) spectrometer (Bruker Vertex Vacuum FTIR). Spectra were collected every 10 minutes at room temperature. The total test duration varied by sample (MK ~3 h, LCC-1 ~7 h, LCC-2 ~8 h, LCC-3 ~5 h), based on early age stiffening. The measurement window was selected to capture the early stages of reaction (stages I–III in SAOS data) and the associated development of the aluminosilicate network, while maintaining consistent spectral quality prior to significant stiffening of the paste.

3. Results and Discussion

3.1 Paste and Precursor Reactivity (IC + MR^3)

Isothermal calorimetry (IC) results presented in Fig. 3a and 3b, establish the extent of early-age polymerization as a function of precursor mineralogy. Among the four mixtures, MK exhibited a characteristic sharp early heat flow peak (Fig. 3a) and the highest cumulative heat release (Fig. 3b). This characteristic rapid dissolution of aluminosilicate species followed by accelerated polycondensation corelates with pMK's high reactive amorphous content (~96%), and finer particle size.

The three LCC precursors represent a range of mineralogical and compositional variability typical of naturally occurring low-grade calcined clays, particularly in terms of impurities, amorphous content, Si/Al ratio, and alkali availability. Among the LCC mixtures, LCC-1 has the highest heat flow, followed by LCC-2 and LCC-3. LCC-1 mixture exhibits a distinct heat flow peak similar in shape to MK, but broader and shifted to later times, indicating that while the underlying reaction pathway remains comparable, the kinetics are more gradual. Its lower heat flow is attributed to pLCC-1's reduced amorphous content (~56%), coarser particle size, and compositional differences in the paste, particularly a higher Si/Al ratio and Na/Al ratio, which limits the availability of reactive aluminates [23], [24], [32], [33].

In contrast, LCC-2 mixture showed both lower reaction rate and overall reaction extent compared to LCC-1, despite comparable particle size and amorphous content of the precursors. Its lower Na/Al ratio (0.74) restricts dissolution and slows oligomer formation [33], while less reactive crystalline phases such as mullite further reduce the effective reactive fraction [34]. LCC-3 mixture

exhibited the lowest overall reaction extent but a relatively faster reaction rate, as indicated by the early plateau in Fig. 3a. This behavior arises from pLCC-3's low amorphous content (~22%) combined with higher Si/Al and Na/Al ratios in the paste, where increased alkali availability promotes rapid initial interactions but limited reactive content restricts sustained reaction.

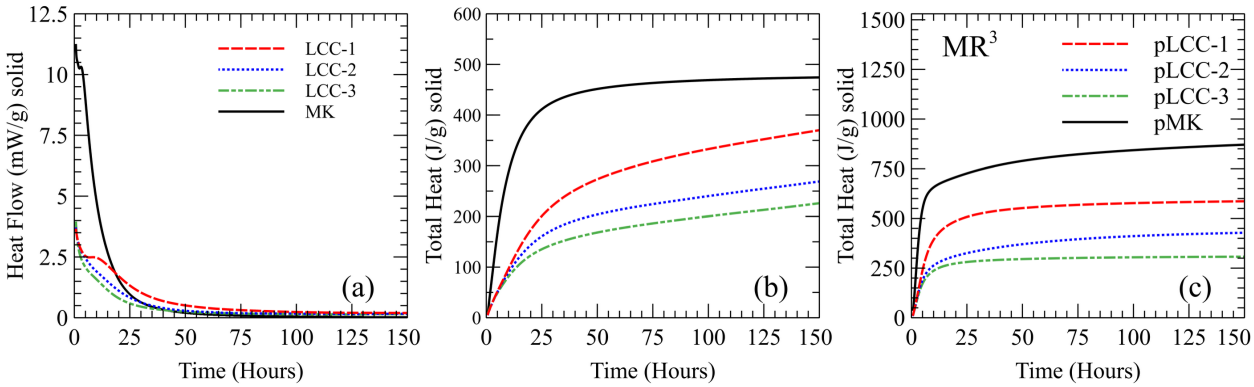

Figure 3: Isothermal calorimetry results showcasing (a) heat flow and (b) cumulative heat of the alkali activated pastes; (c) modified reactivity test (MR^3) of the precursors.

Interestingly, all LCC systems exceeded the MR^3 reactivity threshold (120 J/g) [31], indicating sufficient intrinsic reactive aluminosilicates for consumption of portlandite in OPC systems and potentially for alkali activation. The overall reactivity ranking from Fig. 3c (pMK > pLCC-1 > pLCC-2 > pLCC-3) is governed by a combination of reactive amorphous content, composition, and particle size rather than any single parameter. pMK and pLCC-1 exhibit more defined heat flow peaks, while pLCC-2 and pLCC-3 show subdued responses due to reduced reactivity. MR^3 test is also an indicator for later age reactivity and the results indicate that the pLCC's with initial lower heat release content remain low and do not catchup at later ages.

Finally, cumulative heat for all LCC mixtures did not plateau within the measurement window (Fig. 3b), indicating continued polymerization beyond the testing time. While calorimetry distinguishes reaction rate and extent, it does not directly quantify structural development. To address this, rheological measurements are used to track the structuration in real time.

3.2 Suspension Behavior After Mixing (Flow Curves)

Prior to the onset of significant chemical reaction, the fresh paste behaves as a concentrated suspension where rheological response is governed primarily by particle interactions and the properties of the activating solution. Flow curves for all mixtures (Fig. 4) reveal a critical distinction between high-purity and low-grade precursors. The MK baseline mixture exhibited non-linear, shear-thickening behavior (Fig. 4b, 4c), characterized by a power-law index (n) of 1.3. Notably, this reduced workability occurred despite a significantly higher water-to-binder ratio (w/b = 0.9) compared to the LCC mixtures (w/b = 0.6), highlighting the inherent processing difficulties and extreme water demand associated with pure, high-surface-area metakaolin precursor.

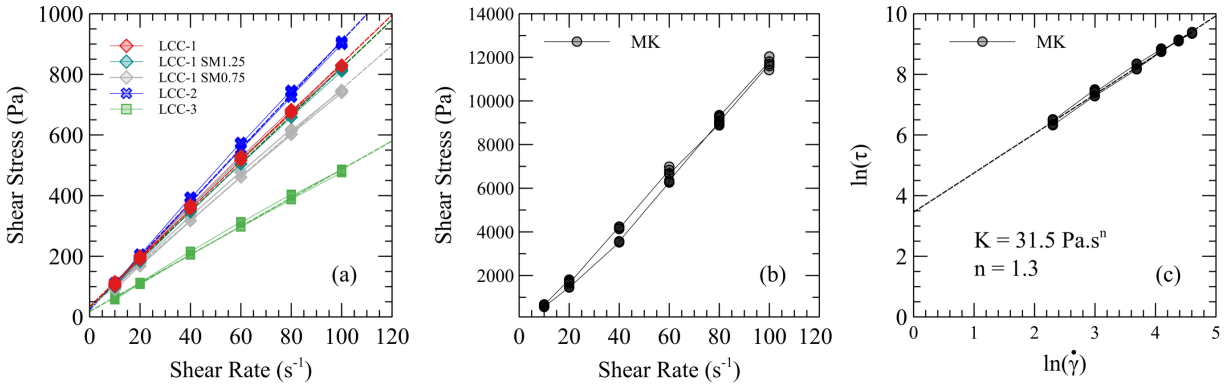

Figure 4: Flow curves for mixtures with (a) LCCs, (b) MK, and (c) MK in log scale with parameters for power-law model.

Table 4: Rheological parameters (yield stress and plastic viscosity) of LCC mixtures.

	Yield Stress (Pa)	Viscosity (Pa.s)
LCC-1	33.8	8.04
LCC-1 SM1.25	31.5	7.90
LCC-1 SM0.75	29.2	7.22
LCC-2	23.2	8.86
LCC-3	18	4.68

In contrast, all LCC mixtures followed a linear Bingham model, allowing for the quantification of yield stress and plastic viscosity (Table 4). A minor hysteresis was observed in these curves, indicating their inherent viscoelastic nature. As the activator and the water content of the different LCC pastes were the same, this effect can be attributed to their particle interaction, water absorption properties and early age chemistry. For the LCC-1 system, reducing the activator silica modulus (SM) from 1.0 to 0.75 resulted in a slight reduction in both yield stress (33 to 29 Pa) and plastic viscosity (6 to 5 Pa.s). However, increasing the SM to 1.25 did not follow the expected trend of increased viscosity; instead, a marginal decrease in both yield stress and viscosity was observed. Additional dissolved silica seemed to introduce complex competing effects which subtly influenced early-age workability of the pastes. Precursor particle size and reactivity, however, remained the dominant parameters governing the overall flow behavior of the pastes.

3.3 Viscoelastic Behavior of AAM Pastes (SAOS Tests)

The transition of alkali-activated pastes from a fluid suspension to a solid, load-bearing network was tracked using SAOD tests. Storage modulus (G′), loss modulus (G″), and phase angle (δ) were monitored within the linear viscoelastic region (1 Hz frequency, 0.01% strain) to reveal the real-time structural development (Figs. 5 – 7). Despite significant mineralogical differences between precursors, all systems exhibited a consistent four-stage viscoelastic evolution.

Stage I corresponds to the initial restructuring of the paste following preshear, where the disrupted particle network begins to recover. During this stage, G′ remains low (≈ 500 - 1000 Pa), and the

response is dominated by particle rearrangement and relaxation. Stage II represents the primary chemical regime, involving dissolution of aluminosilicate species and formation of early oligomeric structures. This stage is characterized by a gradual increase in G′ (≈ 1–3 kPa), reflecting the development of weak structural connectivity while the system remains predominantly fluid-like, as indicated by relatively higher phase angles. Differences between clays become more pronounced here as MK (Fig. 5a) exhibits a temporary drop in G′ and G″, likely due to rapid dissolution and high level of water release (due to polycondensation) disrupting the evolving structure before significant network formation occurs [17]. In contrast, LCC mixtures (Fig. 5b, 5c, 5d) show a gradual and monotonic evolution, consistent with slower and more distributed reaction kinetics.

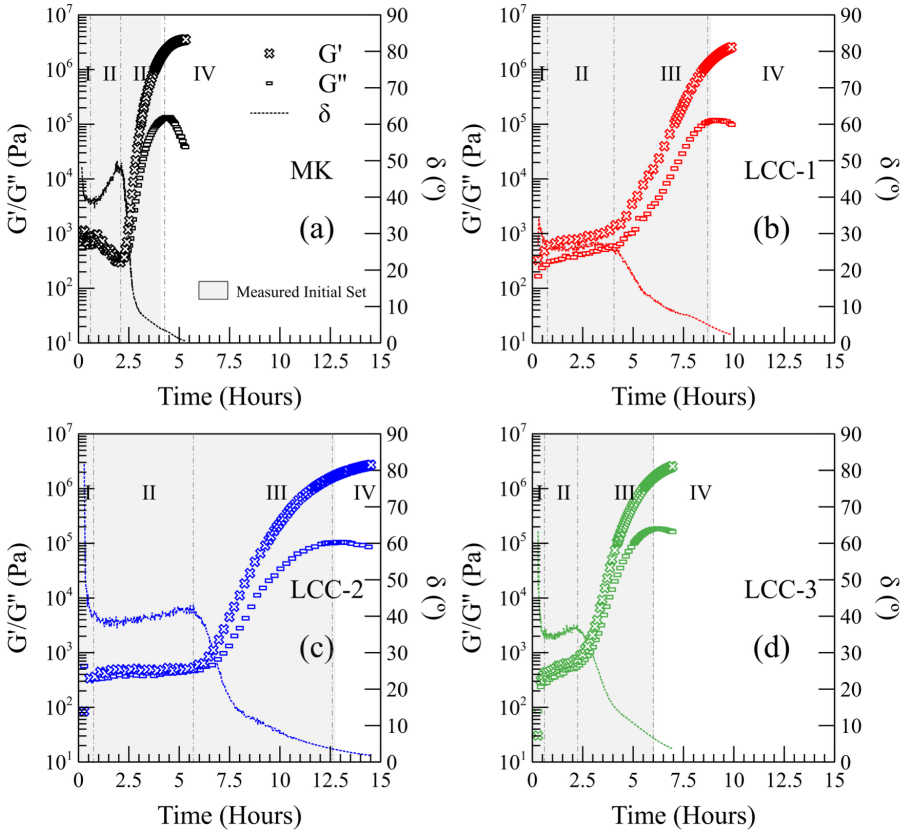

Figure 5: SAOS time sweep tests (a) MK (b) LCC-1 (c) LCC-2 (d) LCC-3. Grey shaded portion represents the Vicat measured initial set time.

Stage III represents the key transition regime, where the system evolves from a weakly structured suspension to a dominantly connected network. This stage is marked by a sharp increase in both G′ and G″, with G′ becoming dominant as solid-like behavior emerges, increasing rapidly from ~1 kPa to nearly 1 MPa. The end of Stage III is defined by the peak in G″, representing the point where viscous dissipation is maximized before the liquid-like behavior diminishes. This point aligns closely (± 20 min) with the initial set time measured using the Vicat method (shaded portion, Fig. 5) [30], and is supported by a diminishing phase angle, confirming the transition to a

predominantly elastic state. While all mixtures exhibit this transition, the rate varies: MK progresses rapidly due to its high reactivity, whereas LCC systems transition more gradually, with LCC-3 showing relatively faster progression despite lower overall reaction extent.

Stage IV reflects the continued polymerization and structural refinement of the now-solidified network. In this stage, G′ continues to increase while G″ decreases rapidly, indicating a progressively more elastic and rigid network. Although the material has already achieved rigidity by the end of Stage III, this stage represents further densification and reorganization of the aluminosilicate network.

Overall, MK exhibited the fastest progression through the stages, consistent with the precursors high amorphous content and finer particle size (Fig. 6a). Among the LCCs, however, LCC-3 showed relatively faster transitions despite lower intrinsic reactivity, likely due to its relatively higher Na/Al ratio (Table 3) enhancing dissolution and early polycondensation. This highlights that while precursor reactivity defines the baseline behavior, the activator to reactive component of the precursor can exert a strong secondary control on kinetics, at times overriding compositional trends. This behavior is further explained in Section 3.4 while monitoring the chemical evolution during stiffening.

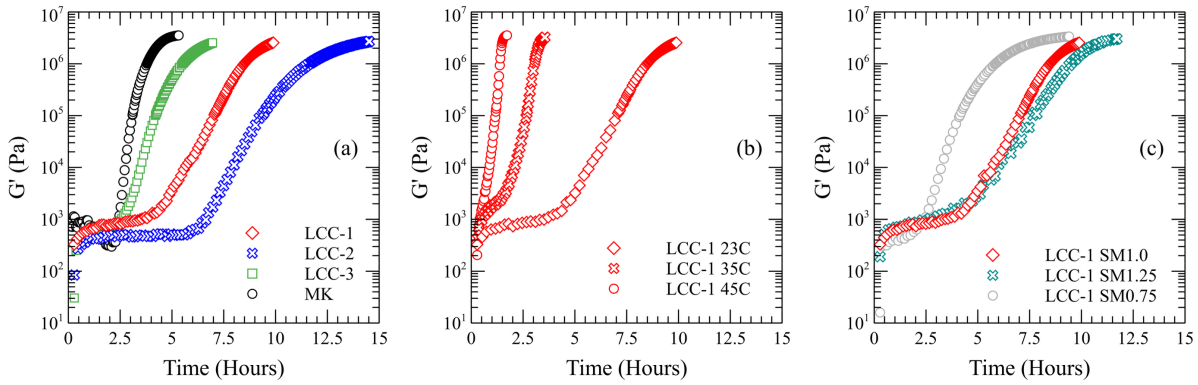

Figure 6: SAOS results summarizing effects of (a) precursor composition, (b) temperature variation (LCC-1), and (c) SM variation (LCC-1).

To further isolate the effects of activator chemistry and curing conditions, the influence of activator silica modulus (SM) and temperature was examined using LCC-1 as a representative system (Fig. 6b, 6c). Variations in SM altered the rate of viscoelastic evolution without changing the overall four-stage pathway. Reducing SM from 1 to 0.75 accelerated progression through Stages II and III and led to earlier setting, primarily due to the higher Na/Al ratio and enhanced dissolution associated with lower-SM activators [23], [24]. In contrast, increasing SM to 1.25 delayed the Stage III despite a slightly faster initial increase in G′ during Stage II, suggesting that higher dissolved silica promotes early short-range structuring but requires greater reorganization before a percolated network can form. Regarding curing temperature, increasing it resulted in accelerating progression through all stages while preserving the overall shape of the response. However, the faster evolution observed at lower SM and higher temperature did not translate into higher

compressive strength (Section 3.5), indicating that rapid stiffening alone is insufficient to produce the strongest network. Instead, slower evolution at higher SM appears to promote improved structural organization prior to rigidification.

3.4 Chemical–Rheological Coupling (FTIR + SAOS)

While SAOS tests captures the evolution of early-age structuration during alkali activation, it does not directly elucidate the chemical transformations responsible for the observed rheological transitions. To establish this connection, *in situ* FTIR was used to monitor the chemical evolution of the reacting pastes and relate these changes to the rheological progression identified in SAOS data.

The evolution of the aluminosilicate network was tracked through changes in the asymmetric Si–O–T (T = Si or Al) vibration region between 850 – 1050 cm^{-1}. This region contains overlapping contributions from dissolved silicate species in the activating solution, unreacted precursor phases, and newly forming aluminosilicate reaction products [35], [36]. Therefore, the broad Si–O–T envelope cannot be assigned to a single vibration or reaction product, particularly in low-grade calcined clays with complex mineralogy. During the early reaction stages (at 20 minutes for all samples in Fig. 7 a-d), two overlapping bands were clearly observed in this region, centered at approximately 920 and 970 cm^{-1}. These bands are associated with silicate species in the activating solution and evolving aluminosilicate environments respectively [37]. As the reaction progressed, the broad Si–O–T envelope peak is observed to evolve towards a more stable band positioned near ~960 cm^{-1}, consistent with progressive aluminosilicate polymerization and formation of a cross-linked reaction product network [38], [39], [40].

Because multiple crystalline and amorphous phases may contribute to this region, complete deconvolution of all possible Si–O–T vibrations would require numerous component bands and could introduce significant fitting uncertainty. Therefore, deconvolution was intentionally limited to the two dominant bands clearly resolved during the early reaction stages. This two-component Gaussian model provided a good representation of the broad Si–O–T envelope throughout reaction, with representative fits typically yielding R^2 values above 0.99. The fitted components are used here as spectral markers of the evolving Si–O–T region. Hereafter, the lower-wavenumber component (Peak 1, Fig. 7), will be referred to as the LW band, while the higher-wavenumber component (Peak 2, Fig. 7), will be referred to as the HW band.

The evolution of the LW band was observed to differ substantially among the different precursors indicating precursor-specific chemical pathways during early activation. To relate this chemical evolution to structural development, the LW band peak position (represented by Peak 1, Fig. 7) was plotted against the corresponding storage modulus, G′, and mapped onto the rheological stage boundaries determined from SAOS (Fig. 8).

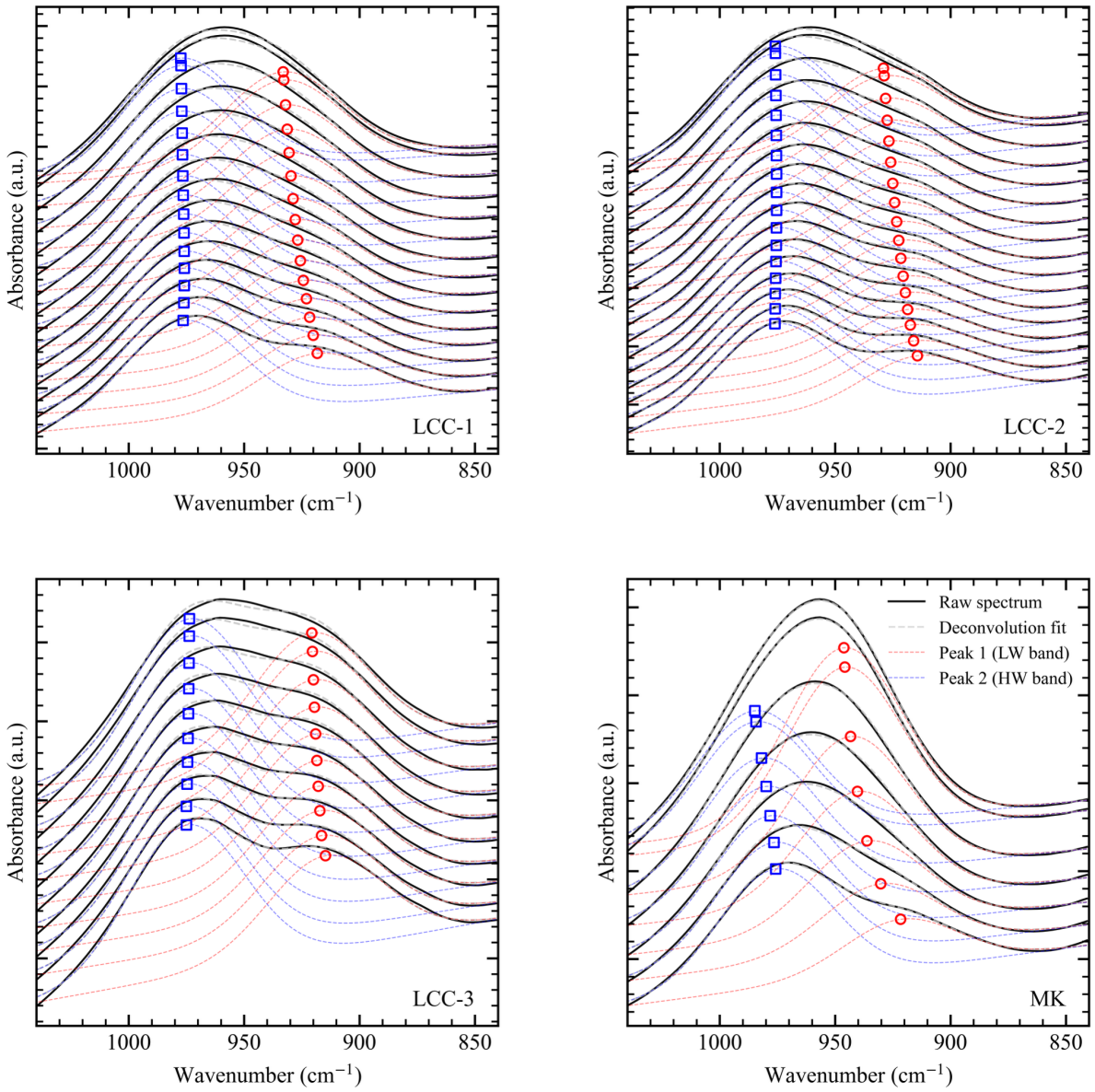

Figure 7: Gaussian deconvolution of the Si–O–T region for the alkali-activated pastes: Low-wavenumber, LW (Peak 1) and high-wavenumber, HW (Peak 2) contributions. Note: All deconvoluted curve fittings have a $R^2 > 0.99$; The absorbance values of the curves have been offset for better clarity.

Across all mixtures, LW band peak shifted substantially during stages I and II while G′ increased only modestly (Fig. 8). This indicates that significant dissolution and oligomer formation occur before the development of a rigid network. In the MK mixture, this decoupling between chemical evolution and stiffness is particularly evident. The LW band peak shifts from ~922 to ~942 cm^{-1} during stage II, yet a temporary decrease in G′ is observed supporting the interpretation that rapid dissolution in MK actively disrupts the early particle network before sufficient reaction products have started forming a rigid structure. In contrast, the LCC systems, particularly the low-amorphous LCC-3, start at a relatively lower wavenumber (< 920 cm^{-1}) and enter stage III after a

much smaller extent of spectral evolution (6 – 10 cm^{-1} shift compared to MK's 20 cm^{-1}). The stage II evolution also helps elucidate the effects of impurities, where highly crystalline impurities like quartz stabilize and improve the rigidity of the network even during dissolution for LCCs whereas the lack of non-reactive impurities is causing disruption of the structure in MK.

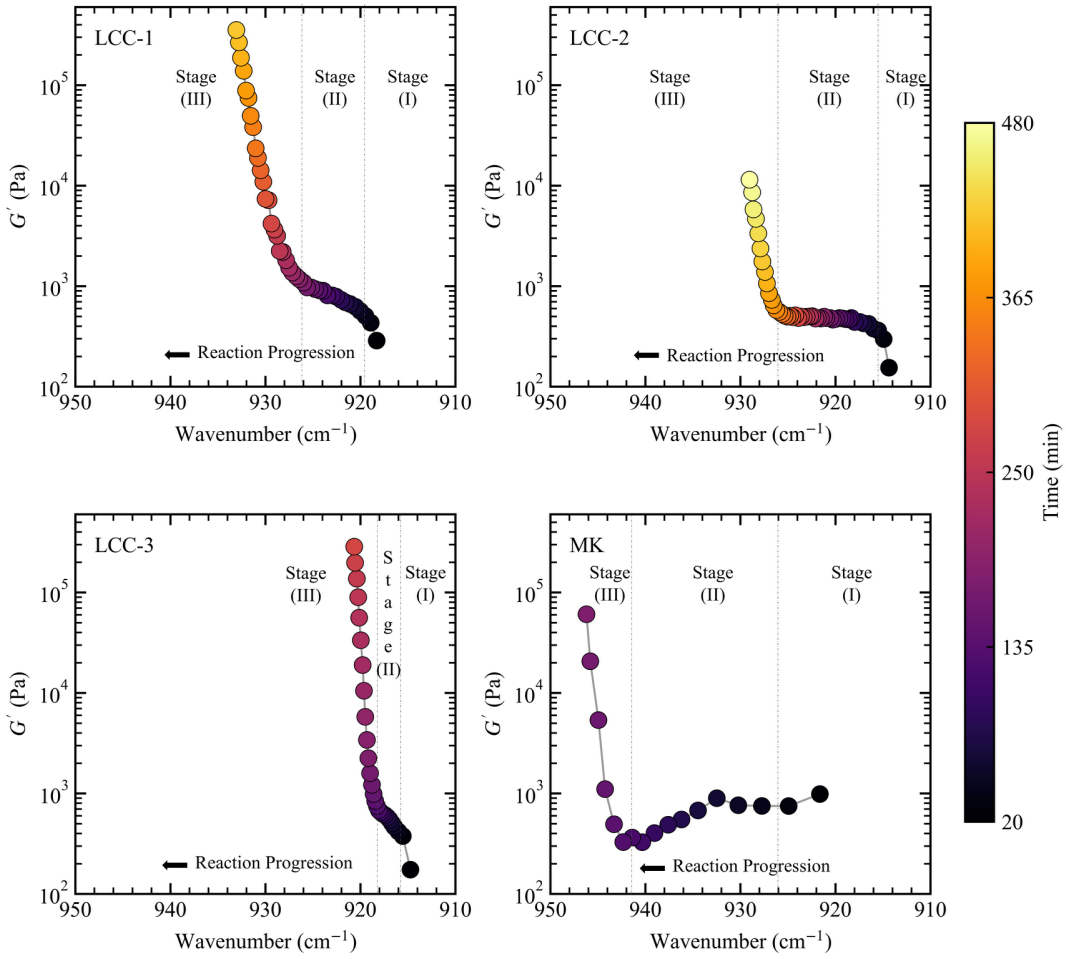

Figure 8: Coupled FTIR-SAOS evolution in time, showing G' as a function of the LW band peak position.

During the transition region (stage III), relatively small additional wavenumber shifts correspond to orders-of-magnitude increases in G′ demonstrating a strongly nonlinear relationship between chemical evolution and stiffening behavior. The shape of the FTIR-SAOS trajectory during stage III reflects the differences in paste reactions. LCC-3 exhibits a steep transition, consistent with limited chemical evolution (low reactivity) followed by rapid stiffening (high Na/Al), whereas LCC-1, LCC-2 and MK show more gradual transitions, indicating continued chemical progression during the development of mechanical rigidity.

Overall, the FTIR-SAOS evolution curves capture the combined effects of precursor composition, crystalline impurities, amorphous fraction, and reactivity on early-age network formation. MK

shows the fastest and largest spectral evolution, consistent with its high amorphous content and fine particle size. Among the LCCs, LCC-1 exhibits the largest chemical transformation, followed by the slower but sustained evolution of LCC-2 and the rapid but more limited transformation of LCC-3. These mechanochemical trajectories provide a characteristic indicator of how different precursors transition from dissolution-dominated chemistry to interconnected stiffer aluminosilicate networks.

3.5 Compressive Strength

The 7-day compressive strengths of the alkali-activated pastes are shown in Fig. 9. For the mixtures prepared with an activator SM of 1, LCC-1 developed the highest strength (41 MPa), followed by MK (36 MPa), while LCC-2 and LCC-3 exhibited progressively lower strengths. The lower strength of MK despite highest intrinsic reactivity is attributed primarily to its poor fresh-state workability and the corresponding high water-to-binder ratio required to produce workable paste. As shown in Fig. 4, MK exhibited strong shear-thickening behavior even at w/b = 0.9, limiting its workability and resulting in a less consolidated hardened structure. This is also reflected in the larger standard deviation of the MK strength compared to the LCC mixtures.

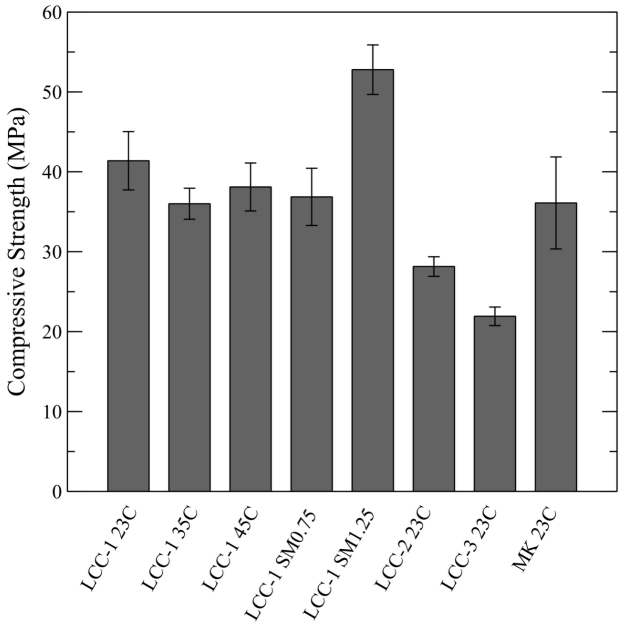

Figure 9: 7-day compressive strengths of all the alkali activated pastes.

Among the LCCs, the strength ranking followed the same order as the chemical reactivity inferred from calorimetry and FTIR, with LCC-1 > LCC-2 > LCC-3 indicating that ultimate strength is governed primarily by the attainable extent of network development rather than by the rate of early reaction alone. LCC-3 progressed through the rheological stages more rapidly than the other LCCs due to higher Na/Al ratio yet developed lower strength because of lower amorphous content limiting the total extent of reaction. Similarly, LCC-2 evolved slower than LCC-1 forming a

weaker network due to its lower intrinsic reactivity. These results show that precursor chemistry, rather than kinetics establishes the strength development that can ultimately be achieved.

The effect of activator chemistry must be considered separately from differences in precursor reactivity. Within a given precursor system, increasing the silica modulus from 0.75 to 1.25 reduced the rate of early evolution but increased compressive strength from 37 to 52 MPa. Combined with the rheological results, this suggests that the higher-silica activator delayed rigidification long enough to allow greater structural organization and refinement prior to the formation of a fully connected network. In contrast, reducing the silica modulus accelerated the transition through Stage III but resulted in lower strength, indicating that rapid early stiffening does not necessarily produce the most favorable final structure.

A similar distinction is observed for curing temperature. Increasing temperature accelerated progression through the rheological stages but did not consistently improve strength. The lower strength observed at 35 °C suggests that excessively rapid network formation may restrict the time available for structural rearrangement and densification prior to rigidification. Thus, while precursor reactivity determines the attainable reaction extent, activator chemistry and curing conditions control how efficiently that potential is translated into a mechanically effective network.

4.0 Conclusion

This study establishes a mechanistic framework for interpreting early-age structural evolution in alkali-activated low-grade calcined clays. Despite differences in composition, amorphous content, impurities, and particle sizes, all systems followed a common four-stage viscoelastic pathway, with precursor chemistry primarily controlling the rate and extent of progression.

SAOS identified Stage III as the critical transition from a weakly structured suspension to a percolated, load-bearing network. The end of this stage, marked by the G″ peak and continued decrease in phase angle, aligned closely with the Vicat initial set. Coupled FTIR-SAOS analysis further showed that chemical evolution and mechanical stiffening are strongly nonlinear. The low-wavenumber Si–O–Si/Al band peak (LW band) from the deconvoluted spectra provided the clearest marker of precursor-specific chemical evolution, whereas the broad envelope and high-wavenumber band showed limited distinction among systems. Substantial LW band shifts occurred during Stages I and II with limited increases in G′, while rapid stiffening occurred only during Stage III after the LW band reached a precursor-dependent transition region.

Intrinsic precursor reactivity controlled the attainable extent of network development, explaining the superior performance of LCC-1 relative to LCC-2 and LCC-3. Total heat from IC proved to be an excellent parameter to compare relative performances in different LCCs with same activators. Within a given precursor system, however, activator chemistry can help control how effectively the reaction potential is translated into strength. Higher silica modulus delayed rigidification but produced the highest strength. In contrast, lower silica modulus and elevated temperature accelerated early evolution without consistently improving strength.

Overall, these findings show that variable low-grade calcined clays can be interpreted through a common structural pathway despite their compositional differences. Linking FTIR markers with SAOS-defined transitions provides a practical framework for understanding the mechanism of alkali-activated LCC binders to design them with improved control over workability, setting, and strength development.

Acknowledgements

The authors thank the Cornell University Duffield College of Engineering for their generous support. This work was also partially supported by the U.S. Department of Energy, Office of Energy Efficiency and Renewable Energy (Award No. DE-EE0011223). The authors thank Prof. Claire White's group (Princeton University), Prof. Maria Juenger's group (The University of Texas at Austin), and Ash Grove Cement Company for the insightful discussions and sourcing of materials. The authors also thank Dr. Fei Yu (Cornell University) for assistance with acquiring the SEM images.

References

[1] B. B. Jindal, T. Alomayri, A. Hasan, and C. R. Kaze, "Geopolymer concrete with metakaolin for sustainability: a comprehensive review on raw material's properties, synthesis, performance, and potential application," *Environ Sci Pollut Res*, vol. 30, no. 10, pp. 25299–25324, Jan. 2022, doi: 10.1007/s11356-021-17849-w.

[2] F. Wang *et al.*, "Metakaolin," in *Properties of Fresh and Hardened Concrete Containing Supplementary Cementitious Materials*, vol. 25, N. De Belie, M. Soutsos, and E. Gruyaert, Eds., in RILEM State-of-the-Art Reports, vol. 25. , Cham: Springer International Publishing, 2018, pp. 153–179. doi: 10.1007/978-3-319-70606-1_5.

[3] J. Davidovits, "Geopolymer Cement a review," *Geopolymer Science and Technics*, vol. Geopolymer Institute Library, no. Technical Paper #21, Jan. 2013, [Online]. Available: www.geopolymer.org

[4] C. Marín-López *et al.*, "Synthesis and characterization of a concrete based on metakaolin geopolymer," *Inorg Mater*, vol. 45, no. 12, pp. 1429–1432, Dec. 2009, doi: 10.1134/S0020168509120231.

[5] K. Sakkas, S. Kapelari, D. Panias, P. Nomikos, and A. Sofianos, "Fire Resistant K-Based Metakaolin Geopolymer for Passive Fire Protection of Concrete Tunnel Linings," *OALib*, vol. 01, no. 06, pp. 1–9, 2014, doi: 10.4236/oalib.1100806.

[6] J. Temuujin, A. Minjigmaa, W. Rickard, M. Lee, I. Williams, and A. Van Riessen, "Preparation of metakaolin based geopolymer coatings on metal substrates as thermal barriers," *Applied Clay Science*, vol. 46, no. 3, pp. 265–270, Nov. 2009, doi: 10.1016/j.clay.2009.08.015.

[7] A. Palomo, M. T. Blanco-Varela, M. L. Granizo, F. Puertas, T. Vazquez, and M. W. Grutzeck, "Chemical stability of cementitious materials based on metakaolin," *Cement and Concrete Research*, vol. 29, no. 7, pp. 997–1004, Jul. 1999, doi: 10.1016/S0008-8846(99)00074-5.

[8] A. Palomo, M. W. Grutzeck, and M. T. Blanco, "Alkali-activated fly ashes," *Cement and Concrete Research*, vol. 29, no. 8, pp. 1323–1329, Aug. 1999, doi: 10.1016/S0008-8846(98)00243-9.

[9] F. Slaty, H. Khoury, H. Rahier, and J. Wastiels, “Durability of alkali activated cement produced from kaolinitic clay,” *Applied Clay Science*, vol. 104, pp. 229–237, Feb. 2015, doi: 10.1016/j.clay.2014.11.037.
[10] D. Zhao and R. Khoshnazar, “Microstructure of cement paste incorporating high volume of low-grade metakaolin,” *Cement and Concrete Composites*, vol. 106, p. 103453, Feb. 2020, doi: 10.1016/j.cemconcomp.2019.103453.
[11] P. Duxson and J. L. Provis, “Designing Precursors for Geopolymer Cements,” *Journal of the American Ceramic Society*, vol. 91, no. 12, pp. 3864–3869, Dec. 2008, doi: 10.1111/j.1551-2916.2008.02787.x.
[12] J. L. Provis and J. S. J. Van Deventer, Eds., *Geopolymers: structure, processing, properties and industrial applications*. in Woodhead Publishing in materials. Oxford : Boca Raton, FL: Woodhead ; CRC Press, 2009.
[13] M. Rowles and B. O’Connor, “Chemical optimisation of the compressive strength of aluminosilicate geopolymers synthesised by sodium silicate activation of metakaolinite,” *J. Mater. Chem.*, vol. 13, no. 5, pp. 1161–1165, Apr. 2003, doi: 10.1039/b212629j.
[14] R. A. Fletcher, K. J. D. MacKenzie, C. L. Nicholson, and S. Shimada, “The composition range of aluminosilicate geopolymers,” *Journal of the European Ceramic Society*, vol. 25, no. 9, pp. 1471–1477, Jun. 2005, doi: 10.1016/j.jeurceramsoc.2004.06.001.
[15] Q. Wan *et al.*, “Geopolymerization reaction, microstructure and simulation of metakaolin-based geopolymers at extended Si/Al ratios,” *Cement and Concrete Composites*, vol. 79, pp. 45–52, May 2017, doi: 10.1016/j.cemconcomp.2017.01.014.
[16] A. S. De Vargas, D. C. C. Dal Molin, A. C. F. Vilela, F. J. D. Silva, B. Pavão, and H. Veit, “The effects of Na2O/SiO2molar ratio, curing temperature and age on compressive strength, morphology and microstructure of alkali-activated fly ash-based geopolymers,” *Cement and Concrete Composites*, vol. 33, no. 6, pp. 653–660, Jul. 2011, doi: 10.1016/j.cemconcomp.2011.03.006.
[17] C. Li, H. Sun, and L. Li, “A review: The comparison between alkali-activated slag (Si + Ca) and metakaolin (Si + Al) cements,” *Cement and Concrete Research*, vol. 40, no. 9, pp. 1341–1349, Sep. 2010, doi: 10.1016/j.cemconres.2010.03.020.
[18] P. Duxson, A. Fernández-Jiménez, J. L. Provis, G. C. Lukey, A. Palomo, and J. S. J. Van Deventer, “Geopolymer technology: the current state of the art,” *J Mater Sci*, vol. 42, no. 9, pp. 2917–2933, May 2007, doi: 10.1007/s10853-006-0637-z.
[19] P. Duxson, G. C. Lukey, and J. S. J. Van Deventer, “Thermal evolution of metakaolin geopolymers: Part 1 – Physical evolution,” *Journal of Non-Crystalline Solids*, vol. 352, no. 52–54, pp. 5541–5555, Dec. 2006, doi: 10.1016/j.jnoncrysol.2006.09.019.
[20] P. Duxson, G. C. Lukey, and J. S. J. Van Deventer, “The thermal evolution of metakaolin geopolymers: Part 2 – Phase stability and structural development,” *Journal of Non-Crystalline Solids*, vol. 353, no. 22–23, pp. 2186–2200, Jul. 2007, doi: 10.1016/j.jnoncrysol.2007.02.050.
[21] P. Duxson, G. C. Lukey, F. Separovic, and J. S. J. Van Deventer, “Effect of Alkali Cations on Aluminum Incorporation in Geopolymeric Gels,” *Ind. Eng. Chem. Res.*, vol. 44, no. 4, pp. 832–839, Feb. 2005, doi: 10.1021/ie0494216.
[22] O. Burciaga-Diaz, J. I. Escalante-Garcia, and A. Gorokhovsky, “Geopolymers based on a coarse low-purity kaolin mineral: Mechanical strength as a function of the chemical composition and temperature,” *Cement and Concrete Composites*, vol. 34, no. 1, pp. 18–24, Jan. 2012, doi: 10.1016/j.cemconcomp.2011.08.001.

[23] L. Weng and K. Sagoe-Crentsil, “Dissolution processes, hydrolysis and condensation reactions during geopolymer synthesis: Part I—Low Si/Al ratio systems,” *J Mater Sci*, vol. 42, no. 9, pp. 2997–3006, May 2007, doi: 10.1007/s10853-006-0820-2.
[24] K. Sagoe-Crentsil and L. Weng, “Dissolution processes, hydrolysis and condensation reactions during geopolymer synthesis: Part II. High Si/Al ratio systems,” *J Mater Sci*, vol. 42, no. 9, pp. 3007–3014, May 2007, doi: 10.1007/s10853-006-0818-9.
[25] J. Davidovits, *Geopolymer: chemistry and applications*. Saint-Quentin: Institut Géopolymère, 2008.
[26] S. N. Abd Bakil, F. Kristály, and G. Mucsi, “Preliminary Study of Low-Grade Clays as Secondary Raw Material for Geopolymer,” *Geosciences and Engineering*, vol. 11, no. 1, pp. 68–84, Oct. 2023, doi: 10.33030/geosciences.2023.01.006.
[27] B. B. Kenne Diffo, A. Elimbi, M. Cyr, J. Dika Manga, and H. Tchakoute Kouamo, “Effect of the rate of calcination of kaolin on the properties of metakaolin-based geopolymers,” *Journal of Asian Ceramic Societies*, vol. 3, no. 1, pp. 130–138, Mar. 2015, doi: 10.1016/j.jascer.2014.12.003.
[28] N. R. Rakhimova *et al.*, “Role of Clay Minerals Content and Calcite in Alkali Activation of Low-Grade Multimineral Clays,” *J. Mater. Civ. Eng.*, vol. 32, no. 8, p. 04020198, Aug. 2020, doi: 10.1061/(ASCE)MT.1943-5533.0003255.
[29] M. F. Alnahhal, T. Kim, and A. Hajimohammadi, “Distinctive rheological and temporal viscoelastic behaviour of alkali-activated fly ash/slag pastes: A comparative study with cement paste,” *Cement and Concrete Research*, vol. 144, p. 106441, Jun. 2021, doi: 10.1016/j.cemconres.2021.106441.
[30] C01 Committee, *Test Methods for Time of Setting of Hydraulic Cement by Vicat Needle*. doi: 10.1520/C0191-21.
[31] P. Suraneni, “Recent developments in reactivity testing of supplementary cementitious materials,” *RILEM Tech Lett*, vol. 6, pp. 131–139, Dec. 2021, doi: 10.21809/rilemtechlett.2021.150.
[32] H. Xu and J. S. J. Van Deventer, “The geopolymerisation of alumino-silicate minerals,” *International Journal of Mineral Processing*, vol. 59, no. 3, pp. 247–266, Jun. 2000, doi: 10.1016/S0301-7516(99)00074-5.
[33] L. Hou, J. Li, and Z. Lu, “Effect of Na/Al on formation, structures and properties of metakaolin based Na-geopolymer,” *Construction and Building Materials*, vol. 226, pp. 250–258, Nov. 2019, doi: 10.1016/j.conbuildmat.2019.07.171.
[34] A. Elimbi, H. K. Tchakoute, and D. Njopwouo, “Effects of calcination temperature of kaolinite clays on the properties of geopolymer cements,” *Construction and Building Materials*, vol. 25, no. 6, pp. 2805–2812, Jun. 2011, doi: 10.1016/j.conbuildmat.2010.12.055.
[35] A. Hajimohammadi, T. Ngo, and J. Vongsvivut, “Interfacial chemistry of a fly ash geopolymer and aggregates,” *Journal of Cleaner Production*, vol. 231, pp. 980–989, Sep. 2019, doi: 10.1016/j.jclepro.2019.05.249.
[36] K. M. L. Alventosa and C. E. White, “The effects of calcium hydroxide and activator chemistry on alkali-activated metakaolin pastes,” *Cement and Concrete Research*, vol. 145, p. 106453, Jul. 2021, doi: 10.1016/j.cemconres.2021.106453.
[37] J. L. Bass and G. L. Turner, “Anion Distributions in Sodium Silicate Solutions. Characterization by^{29} SI NMR and Infrared Spectroscopies, and Vapor Phase Osmometry,” *J. Phys. Chem. B*, vol. 101, no. 50, pp. 10638–10644, Dec. 1997, doi: 10.1021/jp9715282.

[38] S. A. Bernal, R. Mejía De Gutiérrez, and J. L. Provis, "Engineering and durability properties of concretes based on alkali-activated granulated blast furnace slag/metakaolin blends," *Construction and Building Materials*, vol. 33, pp. 99–108, Aug. 2012, doi: 10.1016/j.conbuildmat.2012.01.017.

[39] E. N. Kani and H. Mehdizadeh, "Investigating Gel Molecular Structure and Its Relation with Mechanical Strength in Geopolymer Cement Based on Natural Pozzolan Using In Situ ATR-FTIR Spectroscopy," *J. Mater. Civ. Eng.*, vol. 29, no. 8, p. 04017078, Aug. 2017, doi: 10.1061/(ASCE)MT.1943-5533.0001917.

[40] C. A. Rees, J. L. Provis, G. C. Lukey, and J. S. J. Van Deventer, "In Situ ATR-FTIR Study of the Early Stages of Fly Ash Geopolymer Gel Formation," *Langmuir*, vol. 23, no. 17, pp. 9076–9082, Aug. 2007, doi: 10.1021/la701185g.